

# Reconstruction of HI power spectra with radio-interferometers to study dark energy

R. Ansari<sup>1</sup>, J.-M. Le Goff<sup>2</sup>, Ch. Magneville<sup>2</sup>, M. Moniez<sup>1</sup>, N. Palanque-Delabrouille<sup>2</sup>, J. Rich<sup>2</sup>,  
V. Ruhlmann-Kleider<sup>2</sup> and Ch. Yèche<sup>2</sup>

<sup>1</sup> Laboratoire de l'Accélérateur Linéaire, IN2P3-CNRS, Université de Paris-Sud, BP. 34, 91898 Orsay Cedex, France

<sup>2</sup> CEA, Centre de Saclay, IRFU, F-91191 Gif-sur-Yvette, France

Received June 15, 2008; accepted yyyy xx, 2008

## ABSTRACT

Among the tools available for the study of the dark energy driving the expansion of the Universe, Baryon Acoustic Oscillations (BAO) and their effects on the matter power spectrum are particularly attractive. It was recently proposed to study these oscillations by mapping the 21cm emission of the neutral hydrogen in the redshift range  $0.5 < z < 3$ . We discuss here the precision of such measurements using radio-interferometers consisting of arrays of dishes or north-south oriented cylinders. We then discuss the resulting uncertainties on the BAO scales and the sensitivity to the parameters of the Dark Energy equation of state.

**Key words.** Cosmology – Dark Energy – Baryonic Acoustic Oscillations - radio interferometer - HI

## 1. Introduction

One of the goals of current cosmological research is to fully characterize the “dark energy” that drives the apparent acceleration of the expansion of the Universe. Among the available tools (Albrecht et al. 2006), much interest has been generated by the features in the matter power spectrum that result from Baryon Acoustic Oscillations (BAO) in the pre-recombination Universe. These oscillations cause a peak in the matter correlation function at a comoving distance,  $s \sim 105h^{-1}Mpc$ , equal to the acoustic horizon at recombination. Equivalently, the BAO induce “wiggles” in the matter power spectrum with peaks at comoving wave numbers  $k = (n + 1/2)\pi/s$  for  $n = 2, 4, \dots$ . The theoretical positions of these peaks are known to a precision of order 1% so they can be used as reliable standard rulers to study the expansion history.

After first being seen in the CMB anisotropy spectrum (Mauskopf et al. 2000; Hinshaw et al. 2008), BAO effects were subsequently observed in the low-redshift ( $z < 1$ ) galaxy correlation function and power spectrum by the SDSS survey (Eisenstein et al. 2005; Percival et al. 2007) and the 2dGFRS survey (Cole et al. 2005). With future data in the redshift range  $0.5 < z < 3$ , it is hoped to provide precise constraints on dark-energy parameters. It has been proposed to do this with redshift surveys using galaxy optical spectra (Basset et al. 2005) or HI emission (Abdala & Rawlings 2005) or by mapping in three dimensions the pattern of Lyman- $\alpha$  absorption of distant quasars (Wolf et al. 2005).

An alternative elegant approach was recently proposed by Peterson et al. (2006) and further developed by Chang et al. (2008). They propose to use neutral hydrogen (HI) as a tracer of matter and simply map out the 21cm emission with an angular resolution that is insufficient to detect individual galaxies (where most HI is concentrated) but sufficient to observe the BAO wiggles. At redshift  $z = 1.5$ , the acoustic horizon subtends  $0.0334$ rad on the sky which can be resolved with telescopes of

size of order 100m. These would be considerably smaller and cheaper than the 1km elements necessary to detect individual high redshift galaxies (Abdala & Rawlings 2005).

Mapping the matter distribution using HI 21 cm emission as a tracer has been extensively discussed in literature (e.g. Furlanetto et al. (2006); Tegmark & Zaldarriaga (2008)). Several projects, such as LOFAR (Rottgering et al. 2006) or MWA (Bowman et al. 2007) aim at detecting the reionization epic ( $z \sim 10$ ). Detecting BAO features around  $z \sim 1$  using HI radio emission has also been discussed by Wyithe et al. (2007).

In Section 2 we review the expectations for the HI power spectrum  $P_{HI}(k)$  and its relation to the large-scale structure matter power spectrum  $P_{LSS}(k)$ . Section 3 describes the interferometric observations that are assumed for this study and Section 4 presents a simplified procedure to use these observations to reconstruct the HI power spectrum in a small volume near the zenith. While this procedure is not entirely realistic, it allows us to give estimates of the reconstructed noise power spectrum,  $P_{noi}(k)$  (Fig. 5). Section 5 discusses the problem of subtraction of foreground and background radio sources. Finally, in Section 6 we describe the constraints on the cosmological parameters that can be derived from the determination of the BAO peaks in the power spectrum.

## 2. The HI power spectrum

The mean HI brightness temperature (assumed to be much greater than the CMB temperature) is (Barkana & Loeb 2007)

$$\bar{T}_{HI}(z) = 0.0466mK \frac{(1+z)^2 f_{HI}(z)}{[\Omega_{\Lambda} + (1+z)^3 \Omega_M]^{1/2}} \frac{\Omega_{HI} h_{70}}{3.5 \times 10^{-4}} \quad (1)$$

where  $\Omega_{HI} \sim 3.5 \times 10^{-4}$  (Zwaan et al. 2005) is the current mean cosmological HI density and

$$f_{HI}(z) = \frac{(HI/H)_z}{(HI/H)_{z=0}} \quad (2)$$

is the fraction of hydrogen in atomic form relative to this fraction at  $z = 0$ . Studies of Lyman- $\alpha$  absorption (Wolf et al. 2005) indicate the  $f_{HI}(z = 1.5) \sim 3$  implying  $\bar{T}_{HI}(z = 1.5) = 0.00033K$ . This is three orders of magnitude below the brightness of extragalactic radio source emission,  $\sim 3400Jy sr^{-1}$ , corresponding to  $\bar{T}_{rs} \sim 0.3K$ . However, these sources, as well as Milky Way emission and CMB radiation, have smooth frequency distributions, allowing them, in principle, to be subtracted.

We are interested in the spatial variations of the HI temperature about the mean. Consider a small cube of volume  $V$  at mean redshift  $z$  corresponding to a HI frequency  $\nu = \nu_0/(1+z)$ . The cube covers a solid angle  $\Delta\Omega = \Delta\alpha \times \Delta\delta$  ( $\alpha = r.a.$ ,  $\delta = dec.$ ) and redshift range  $\Delta z$  corresponding to a frequency range  $\Delta\nu = \nu_0\Delta z/(1+z)^2$ . The present volume of the cube is

$$V = d_T^2 d_H \Delta\Omega \Delta z = \frac{(c/H_0)d_T^2 \Delta\Omega \Delta z}{\sqrt{\Omega_\Lambda + \Omega_M(1+z)^3}} \quad (3)$$

where for a flat  $\Lambda$ CDM universe, the comoving angular distance  $d_T$  and Hubble distance  $d_H$  are

$$d_T = \int_0^z \frac{(c/H_0) dz}{\sqrt{\Omega_\Lambda + \Omega_M(1+z)^3}} \quad d_H = \frac{c/H_0}{\sqrt{\Omega_\Lambda + \Omega_M(1+z)^3}}.$$

Inside the cube, the sky brightness can be expanded using functions that satisfy periodic boundary conditions. For small cubes ( $\Delta\alpha, \Delta\delta, \Delta z \ll 1$ ) the functions can be taken to be complex exponentials of  $(\alpha, \delta, z)$ :

$$T_{HI}(\alpha, \delta, z) = \frac{\bar{T}_{HI}}{\sqrt{V}} \sum_{\mathbf{n}} \Gamma_{HI}(\mathbf{n}) e^{2\pi i(n_\alpha \alpha / \Delta\alpha + n_\delta \delta / \Delta\delta + n_z z / \Delta z)} \quad (4)$$

where the  $\Gamma_{HI}(\mathbf{n} = (n_\alpha, n_\delta, n_z))$ , are defined for integer  $n_\alpha, n_\delta, n_z$ . The wave vector  $\mathbf{k}$  is related to  $\mathbf{n}$  by

$$k_\alpha = \frac{2\pi n_\alpha}{d_T \Delta\alpha} \quad k_\delta = \frac{2\pi n_\delta}{d_T \Delta\delta} \quad k_z = \frac{2\pi n_z}{d_H \Delta z} \quad (5)$$

The HI power spectrum is:

$$P_{HI}(k) = \langle |\Gamma_{HI}(\mathbf{k})|^2 \rangle \quad (6)$$

the average being over the modes  $\mathbf{k}$  with wave numbers near  $k$ . The number of such modes in the cube and in the interval  $\Delta k$  is:

$$\begin{aligned} N_{\Delta k} &= \frac{V k^3}{4\pi^2} \frac{\Delta k}{k} = \frac{(c/H_0)d_T(z)^2 \Delta\Omega \Delta z k^3}{4\pi^2 [\Omega_\Lambda + (1+z)^3 \Omega_M]^{1/2}} \frac{\Delta k}{k} \\ &= 7.25 \times 10^4 \left( \frac{d_T(z)}{c/H_0} \right)^2 \frac{\Delta\Omega \Delta z}{2\pi/5} \left( \frac{k}{0.075 h Mpc^{-1}} \right)^3 \frac{\Delta k/k}{0.2} \\ &\quad \times [\Omega_\Lambda + (1+z)^3 \Omega_M]^{-1/2} \quad (7) \end{aligned}$$

Since the  $|\Gamma(k)|^2$  are random number with variance equal to  $P(k)$  the precision with which  $P(k)$  can be measured is  $P(k)/\sqrt{N_{\Delta k}}$ .

The HI power spectrum is expected to be similar to the galaxy power spectrum. Figure 5 shows the expected galaxy spectrum normalized to agree with that measured by SDSS at  $z \sim 0.1$  (Tegmark et al. 2004). Also shown is this spectrum extrapolated to  $z = 1.5$  assuming  $\Omega_M, \Omega_\Lambda = 0.27, 0.73$ . The spectrum has BAO peaks at

$$k_n = (n + 1/2)\pi/s = 0.075 h Mpc^{-1} \frac{n + 1/2}{2.5} \quad n = 2, 4, 6, \dots \quad (8)$$

where  $s = 105 h^{-1} Mpc$  is the sound horizon at recombination. The relative crest to trough amplitudes at the first three peaks are expected to be  $\Delta P/P \sim 0.13$ ,  $\Delta P/P \sim 0.09$ , and  $\Delta P/P \sim 0.05$ .

### 3. Interferometric Observations

Observations of GHz radiation can be performed with interferometers consisting of arrays of reflectors and receivers. In this paper, we consider two types of arrays. The first, drawn schematically in Fig. 1, consist of north-south oriented cylindrical reflectors pointing towards the zenith. The reflectors have dipole receiving antennae deployed along their axes. The information to be extracted from a pair of such cylinders is illustrated in Fig. 1. The amplitude for each receiver is sampled over a time  $t_{int}$  after which a Fast-Fourier Transform (FFT) is performed to separate frequency components. We take  $t_{int}$  to be sufficiently long ( $\sim 35\mu sec$ ) to give excellent resolution on the BAO features in the radial direction. The receivers within a given cylinder are then combined by a FFT to form beams covering pixels in declination of width  $\sim \lambda/D_\delta$  for a wavelength  $\lambda$  and cylinder length  $D_\delta$ . This requires that receivers be spaced by  $\lambda/2$  in order to avoid large side-lobe contamination. The number of receivers per cylinder is thus of order 500 for  $D_\delta = 100m$ . The amplitudes from two cylinders separated in  $\mathbf{u}\lambda$  in the east-west direction can then be correlated to form a ‘‘visibility’’,  $V(\alpha(t), \delta, \nu, \mathbf{u})$  that is defined for discrete values of declination,  $\delta$ , and frequency,  $\nu$ , defined by the two FFT’s. The right ascension,  $\alpha(t)$  is defined by the time of observation,  $t$ .

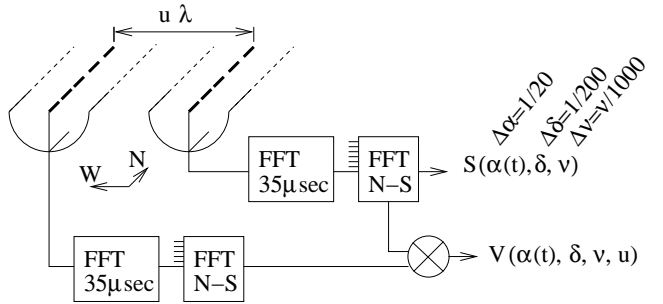


**Fig. 1.** Two cylinders instrumented with dipole receiving antennae along their axes. After a sampling time  $t_{int}$  (taken here to be  $35\mu sec$ ), an FFT is performed for each receiver to separate frequency,  $\nu$ , components. Receivers within a given cylinder are then combined by (north-south) FFT to form beams in declination,  $\delta$ . The amplitudes from the two cylinders can then be combined to form visibilities,  $V(\alpha(t), \delta, \nu, \mathbf{u})$  where  $\alpha(t)$  is the right-ascension determined by the time of the observation and where the cylinder separation is  $\mathbf{u}\lambda$ .

The second type of array considered in this paper consists of dishes that are orientable in declination. The readout for pairs of dishes is the same as for the cylinders in Figure 1 except that there is no north-south FFT so that the declination  $\delta$  is defined by the common dish pointing. Additionally, the dish separation has components in the north-south and east-west directions so  $\mathbf{u}$  is a vector.

The cylinders of Fig. 1 give high resolution information in the declination and frequency directions. In order to provide high quality information in the right-ascension direction, it is necessary to have several cylinders with a range of reflector separations  $\lambda\mathbf{u}$ . Schematics of the three arrays considered here are shown in Figure 2. Two arrays,  $a$  and  $b$ , are arrays of fixed cylindrical reflectors of width  $D_\alpha = 10m$  and length  $D_\delta = 100m$ . The east-west configuration of the five cylinders in configuration  $a$  is chosen to give uniform sensitivity over the  $k$  range necessary for BAO studies. As such, they are placed at positions that are inte-

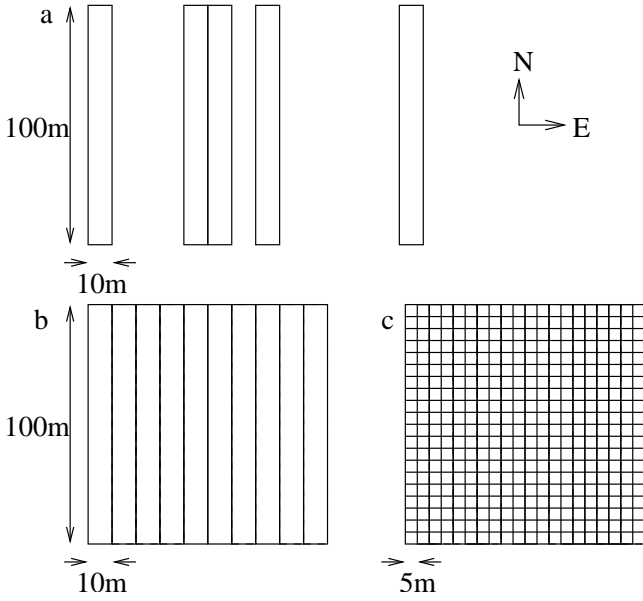


**Fig. 2.** The three telescope configurations considered: a: “unpacked cylinders”; b: “packed cylinders”; c: “packed dishes”. In the unpacked array, the five cylinders are separated from the most western cylinder by distances of  $n \times 10m$  with  $n = 0, 4, 5, 7, 13$ .

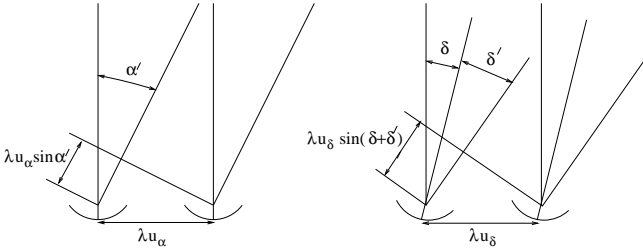


**Fig. 3.** The pointing configuration of telescope pairs (at the terrestrial equator for simplicity). The left panel shows two cylinders separated in the east-west direction and pointing toward the zenith. The right panel shows two dishes separated in the north-south direction and pointing in a direction  $\delta$  from the zenith.

gral multiples of the cylinder width as shown in the figure. On the other hand, the ten cylinder in configuration *b* are adjacent to form a “packed array” giving redundant information over the interesting  $k$  range.

The third system, *c*, is an array of  $D_\alpha \times D_\delta = 5m \times 5m$  dishes (taken to be squares for mathematical convenience). Each dish is instrumented with one receiver. The field-of-view in both angular directions is  $\sim \lambda/D_\alpha$ . In order to survey the sky, the dishes must be pointable in declination. As for the cylinder arrays, the right-ascension is determined by the time of observation.

As illustrated in Fig. 1, each readout-FFT sequence generates a set of amplitudes  $S_{adfc}$  indexed by the four integers:  $a$  giving the right ascension,  $\alpha_a$ , determined by the time of observation;  $(d, f)$  denoting the set of amplitudes generated by FFT corresponding to pixels in declination-frequency space centered on  $\delta_d, \nu_f$  (only one  $d$  per readout for dishes); and  $c$  defining the reflector (dish or cylinder). The amplitudes are the sum of signal and noise:

$$S_{adfc} = S_{adfc}^{noi} + S_{adfc}^{sig} \quad (9)$$

The angular and frequency response are determined by the lobe functions,  $L_{adfc}(\alpha', \delta', \nu')$ , peaked at  $\alpha' = \delta' = \nu' = 0$  and normalized so that the expectation value of the squared signal is

$$\langle |S_{adfc}^{sig}|^2 \rangle = \int d\alpha' d\delta' d\nu' L(\alpha', \delta', \nu') T(\alpha' + \alpha_a, \delta' + \delta_d, \nu' + \nu_f)$$

For the rest of this note we make the approximation that  $L_{adfc}$  is independent of  $(a, d, f, c)$ . The noise contribution is normalized so that the mean signal-to-noise is given by  $\bar{T}/T_{sys}$

$$\langle |S_{adfc}^{noi}|^2 \rangle = T_{sys} \int d\alpha' d\delta' d\nu' L(\alpha', \delta', \nu') \quad (10)$$

The visibility for direction  $(a, d)$  and frequency  $f$  for cylinders (or dishes)  $c$  and  $c'$  separated in space by  $\mathbf{u}\lambda_f$  is:

$$V_{adfu} = S_{adfc} S_{adfc'}^* \quad (11)$$

The noise-noise contribution is a random number of vanishing mean and variance determined by  $T_{sys}$ :

$$\langle |V_{adfu}^{noi}|^2 \rangle^{1/2} = T_{sys} \int d\alpha' d\delta' d\nu' L(\alpha', \delta', \nu') \quad (12)$$

Following Fig. 3, the signal-signal contribution to the visibility has an expectation value

$$\langle V_{adfu}^{sig} \rangle = \int d\alpha' d\delta' d\nu' L(\alpha', \delta', \nu') T(\alpha' + \alpha_a, \delta' + \delta_d, \nu' + \nu_f) \times \exp[-2\pi i(u_\alpha \sin \alpha' + u_\delta \sin(\delta_d + \delta'))] \quad (13)$$

For  $\alpha', \delta' \ll 1$  and  $\delta_d \ll 1$  this simplifies to

$$\langle V_{adfu}^{sig} \rangle e^{2\pi i u_\delta \delta_d} = \int d\alpha' d\delta' d\nu' L(\alpha', \delta', \nu') T(\alpha' + \alpha_a, \delta' + \delta_d, \nu' + \nu_f) e^{-2\pi i \mathbf{u} \cdot \boldsymbol{\theta}} \quad (14)$$

where  $(\boldsymbol{\theta} = (\alpha', \delta'))$ .

#### 4. Reconstruction of HI Power spectrum

The visibilities,  $V_{adfu}$  can be combined to give information on the HI distribution. For a given readout, a Fourier transform of  $V_{adfu}$  over  $\mathbf{u}$  yields a map of the field of view. We are more interested in the power spectrum which is related to the Fourier transform of  $V_{adfu}$  over right-ascension, declination and frequency:

$$\tilde{V}(\mathbf{k}, \mathbf{u}) \equiv \frac{1}{N_d N_f N_a} \sum_{adf} e^{-i(d r k_\alpha \alpha_a + d r k_\delta \delta_d + d_H k_z z_f)} V_{adfu} e^{2\pi i u_\delta \delta_d} \quad (15)$$

where there are  $N_d \times N_f \times N_a$  pixels densely and uniformly covering the cube  $(\Delta\alpha, \Delta\delta, \Delta\nu)$ . In the absence of noise, substituting the expansion (4) into (14) shows that  $\tilde{V}(\mathbf{k}, \mathbf{u})$  is proportional to the product of  $\Gamma_{HI}(\mathbf{k})$  and the Fourier transform of the lobe function. More generally, the visibilities are due to noise and signal so we have

$$\tilde{V}(\mathbf{k}, \mathbf{u}) = \frac{\bar{T}\Gamma(\mathbf{k}) F(\mathbf{k}, \mathbf{u})}{\sqrt{V}} \int d\alpha' d\delta' d\nu' L(\alpha', \delta', \nu') \quad (16)$$

where  $\Gamma(\mathbf{k}) = \Gamma_{HI}(\mathbf{k}) + \Gamma_{noi}(\mathbf{k})$  (plus foreground/background contributions) and where the dimensionless “form factor” for the mode  $\mathbf{k}$  is

$$F(\mathbf{k}, \mathbf{u}) = \frac{\int d\alpha' d\delta' d\nu' L(\alpha', \delta', \nu') e^{i k_z d_H (1+z)^2 \nu'} e^{i \boldsymbol{\theta}' \cdot (d r \mathbf{k} - 2\pi \mathbf{u})}}{\int d\alpha' d\delta' d\nu' L(\alpha', \delta', \nu')} \quad (17)$$

If  $L$  is symmetric,  $F$  is a real function.

The estimate of  $\Gamma(\mathbf{k})$  based on the visibility of one reflector pair with separation  $\mathbf{u}$  is denoted  $\Gamma(\mathbf{k}, \mathbf{u})$ . From (16), it is given by

$$\Gamma(\mathbf{k}, \mathbf{u}) = C \frac{\tilde{V}(\mathbf{k}, \mathbf{u})}{F(\mathbf{k}, \mathbf{u})} \quad (18)$$

where the ‘‘calibration constant’’,  $C$ , relates the power spectrum to the measurements and form factors:

$$C = \frac{\sqrt{V}}{\bar{T} \int d\alpha' d\delta' d\nu' L(\alpha', \delta', \nu')} \quad (19)$$

Since more than one value of  $\mathbf{u}$  can be used to estimate  $\Gamma(\mathbf{k})$ , one can make a weighted average of the  $\Gamma(\mathbf{k}, \mathbf{u})$  derived with (18). In the next subsection, we will show that the noise power is inversely proportional to  $F(\mathbf{k}, \mathbf{u})$  so it is reasonable to have weights that are increasing functions of  $|F(\mathbf{k}, \mathbf{u})| \sim F(\mathbf{k}, \mathbf{u})$ . It is most convenient to take the weights to be equal to  $F(\mathbf{k}, \mathbf{u})$ :

$$\Gamma(\mathbf{k}) = \frac{\sum_{\mathbf{u}} F(\mathbf{k}, \mathbf{u}) \Gamma(\mathbf{k}, \mathbf{u})}{\sum_{\mathbf{u}} F(\mathbf{k}, \mathbf{u})} = C \frac{\sum_{\mathbf{u}} \tilde{V}(\mathbf{k}, \mathbf{u})}{\sum_{\mathbf{u}} F(\mathbf{k}, \mathbf{u})} \quad (20)$$

where the sum is over those values of  $\mathbf{u}$  with  $F(\mathbf{k}, \mathbf{u}) \neq 0$  (Other choices of weighting may give slightly lower noise power but at the price on introducing wiggles in the noise power spectrum.)

#### 4.1. The noise

The noise contribution to the  $\tilde{V}(\mathbf{k}, \mathbf{u})$  (15) is the mean of  $N_a N_d N_f$  random numbers of variance given by (12). This gives  $\langle \tilde{V}_{noi}(\mathbf{k}, \mathbf{u}) \rangle = 0$  and

$$\langle |\tilde{V}_{noi}(\mathbf{k}, \mathbf{u})|^2 \rangle^{1/2} = \frac{\langle |V_{adfu}^{noi}|^2 \rangle^{1/2}}{\sqrt{N_a N_d N_f}} \quad (21)$$

The noise,  $\Gamma_{noi}(\mathbf{k}, \mathbf{u})$  reconstructed using (18) is inversely proportional to  $F(\mathbf{k}, \mathbf{u})$  with an expectation value,  $P_0$ , given by

$$P_0 \equiv \langle |\Gamma_{noi}(\mathbf{k}, \mathbf{u}) F(\mathbf{k}, \mathbf{u})|^2 \rangle = \frac{T_{sys}^2}{\bar{T}^2} \frac{V}{N_d N_f N_a}. \quad (22)$$

The survey volume to pixel ratio  $V/N_a N_d N_f$  depends on the interferometer configuration. In all cases the number of pixels along the frequency direction is  $N_f = t_{int} \Delta\nu$  where  $t_{int}$  is the integrating time between electronic readouts. In the angular directions, cylinders and dishes differ. Dishes have only one angular beam, so we have  $N_a N_d = t_{tot}/t_{int}$  where  $t_{tot}$  is the total observation time of the survey. Cylinders, with FFT beam-forming, have  $N_a = t_{tot}/t_{int}$  and  $N_d = \Delta\delta/(\lambda/D_\delta)$  where  $D_\delta$  is the cylinder length. Combining with (3) this gives

$$\begin{aligned} \frac{V}{(1+z)^2 N_a N_d N_f} &= \frac{d_T^2 d_H \Delta\Omega}{t_{tot} \nu_0} \text{ (dishes)} \\ &= \frac{d_T^2 d_H \Delta\Omega}{t_{tot} \nu_0} \frac{\lambda/D_\delta}{\Delta\delta} \text{ (cylinders)} \end{aligned} \quad (23)$$

The values of  $P_0$  thus differ for cylinders and dishes. For cylinders we have

$$\begin{aligned} P_0 &= 2.4 \times 10^4 (h^{-1} Mpc)^3 \left( \frac{T_{sys}}{50K} \right)^2 \left( \frac{d_T}{c/H_0} \right)^2 \left( \frac{\lambda/D_\delta}{0.525/100} \right) \\ &\times \left( \frac{\Delta\alpha/t_{tot}}{2\pi/3 \times 10^7 sec} \right) \frac{\sqrt{\Omega_\Lambda + \Omega_M(1+z)^3}}{(1+z)^2 f_{HI}(z)^2} \left( \frac{\Omega_{HI} h_{70}}{3.5 \times 10^{-4}} \right)^{-2} \end{aligned} \quad (24)$$

For dishes we have a much larger  $P_0$  because of the smaller sky coverage:

$$\begin{aligned} P_0 &= 4.6 \times 10^6 (h^{-1} Mpc)^3 \left( \frac{T_{sys}}{50K} \right)^2 \left( \frac{d_T}{c/H_0} \right)^2 \\ &\times \left( \frac{\Delta\Omega/t_{tot}}{2\pi/3 \times 10^7 sec} \right) \frac{\sqrt{\Omega_\Lambda + \Omega_M(1+z)^3}}{(1+z)^2 f_{HI}(z)^2} \left( \frac{\Omega_{HI} h_{70}}{3.5 \times 10^{-4}} \right)^{-2} \end{aligned} \quad (25)$$

Using (20), the expectation value of the noise for the mode  $\mathbf{k}$  is

$$\langle |\Gamma_{noi}(\mathbf{k})|^2 \rangle = \frac{P_0 N_u(\mathbf{k})}{(\sum_{\mathbf{u}} |F(\mathbf{k}, \mathbf{u})|)^2} = \frac{P_0}{N_u(\mathbf{k}) \langle |F(\mathbf{k}, \mathbf{u})| \rangle_u^2} \quad (26)$$

where  $P_0$  is given by (24) or (25) and  $N_u(\mathbf{k})$  is the number of visibilities available for estimating  $\Gamma(\mathbf{k})$ . The noise is thus inversely proportional to  $N_u(\mathbf{k}) \langle F \rangle^2$ . We will see that the large value of  $P_0$  for dishes compared to cylinders will be compensated for by the larger value of  $N_u$ .

#### 4.2. The form factor

To estimate the form factor, we use the lobe function

$$L(\alpha', \delta', \nu') = \left( \frac{\sin \pi \alpha' D_\alpha / \lambda}{\alpha'} \right)^2 \left( \frac{\sin \pi \delta' D_\delta / \lambda}{\delta'} \right)^2 \left( \frac{\sin \pi \nu' t_{int}}{\nu'} \right)^2$$

For a cylinder,  $D_\alpha$  is the width,  $D_\delta$  is the length, and  $t_{int}$  is the integrating time. This lobe function is a reasonable approximation both for the diffraction limited beam in right-ascension and for the FFT formed beams in declination and frequency (if high frequency components are filtered out). The form factor for this lobe is a product of triangle functions  $\Lambda(x)$  ( $\Lambda(0) = 1$ ,  $\Lambda(x) = 0$  for  $|x| > 1$ ). For  $t_{int} > 30 \mu sec$ , the frequency lobe is sufficiently narrow that its Fourier transform is near unity for interesting values of  $k$ . In this case, the form factor is the product of the two angular factors:

$$F(\mathbf{k}, \mathbf{u}) = \Lambda\left(\frac{d_T k_\alpha / 2\pi - u_\alpha}{D_\alpha / \lambda}\right) \Lambda\left(\frac{d_T k_\delta / 2\pi - u_\delta}{D_\delta / \lambda}\right) \quad (27)$$

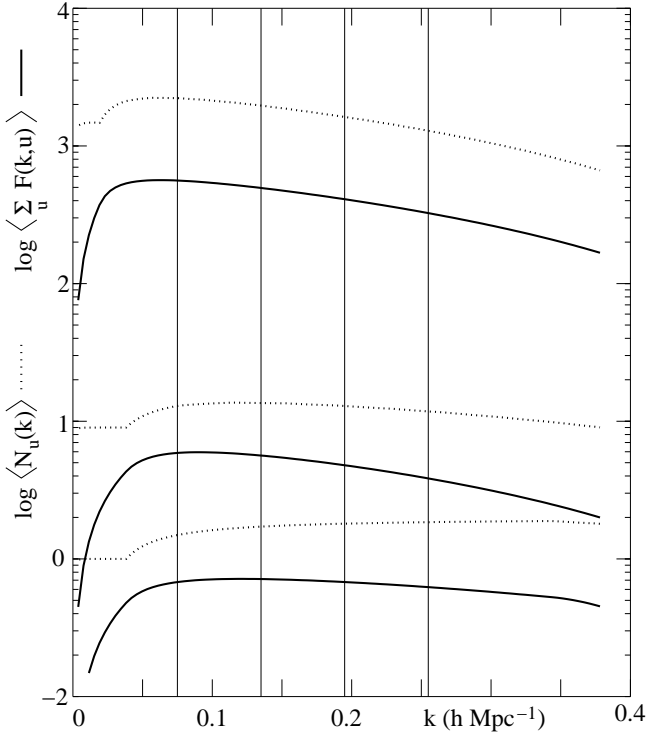
For cylinder arrays,  $u_\delta = 0$ . The most important characteristic of this form factor is that it vanishes as  $k \rightarrow 0$  (i.e.  $k \ll 2\pi D_\alpha / \lambda d_T$ ). This is because only correlations between separated pairs of cylinders are used (no self-correlations) which makes the technique insensitive to noise drifts but at the price of insensitivity to structure on high angular scales. Because of the triangular form of the form factor, for the unpacked cylinder array, there are generally two values of  $u_\alpha$  that have non-vanishing  $F(\mathbf{k}, \mathbf{u})$  for a given  $\mathbf{k}$ : the ones with  $u_\alpha$  just above and just below  $k_\alpha / [2\pi D_\alpha / (\lambda d_T)]$ . For the other two arrays, there are more than two combinations.

Figure 4 plots  $N_u(\mathbf{k})$  and  $\sum_{\mathbf{u}} F(\mathbf{k}, \mathbf{u})$  averaged over orientation of  $\mathbf{k}$  for the three telescope configurations. The dish array has many more pairs for a given  $\mathbf{k}$  than the cylinder array and this works to compensate for its higher noise.

#### 4.3. The power spectrum

The power spectrum  $P(k) = P_{LSS} + P_{noi}$  can be found by calculating a weighted average of the  $|\Gamma(\mathbf{k})|^2$  for  $k$  in an interval  $\Delta k$ :

$$P(k) = \frac{\sum_{\mathbf{k}} W(\mathbf{k}) |\Gamma(\mathbf{k})|^2}{\sum_{\mathbf{k}} W(\mathbf{k})} \quad (28)$$



**Fig. 4.**  $\sum_u F(\mathbf{k}, \mathbf{u})$  (solid lines) and  $N_u(\mathbf{k})$  (dotted lines) both averaged over the orientation of  $\mathbf{k}$ . The top pair of curves is for the dish array (configuration *c* in Figure 2), the middle pair for the packed cylinder array (configuration *b* in Figure 2), the bottom pair for the unpacked cylinder array (configuration *a* in Figure 2). The vertical lines give the positions of the first four BAO peaks.

where  $\Gamma(\mathbf{k})$  is given by (20). A reasonable choice is  $W(\mathbf{k}) = (\sum_u F(\mathbf{k}, \mathbf{u}))^2$  in which case

$$P(k) = \frac{\sum_k |\sum_u F(\mathbf{k}, \mathbf{u}) \Gamma(\mathbf{k}, \mathbf{u})|^2}{\sum_k (\sum_u F(\mathbf{k}, \mathbf{u}))^2} \quad (29)$$

Using (26) we find a simple expression for the noise:

$$P_{noi}(k) = \frac{P_0 \langle N_u(\mathbf{k}) \rangle}{\langle (\sum_u F(\mathbf{k}, \mathbf{u}))^2 \rangle} \quad (30)$$

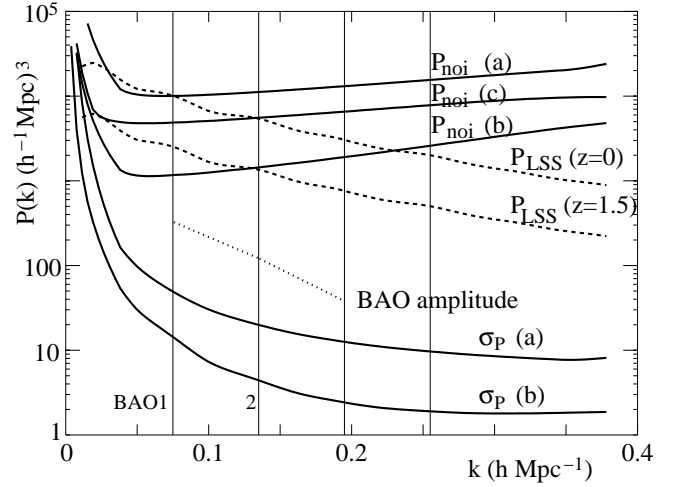
where the averages are over  $\mathbf{k}$ . As expected from (26),  $P_{noi}(k)$  is inversely proportional to  $N_u(\mathbf{k})$ .

Figure 5 shows the  $P_{noi}(k)$  calculated in the three configurations for a four-month observation of  $2\pi sr$  at  $z = 1.5$  ( $\Delta z = 0.2$ ). The noise for the packed array is considerably smaller than that for the unpacked array because of the higher value of  $N_u$ . The larger value of  $P_0$  for the dishes is compensated by the larger value of  $N_u$  so the noise is comparable to that for the cylinder arrays. Note that the dishes accomplish this with fewer electronics channels, 400, than the 2500 (5000) channels needed for the unpacked (packed) cylinders.

For all configurations, the noise diverges as  $k \rightarrow 0$  because of the filtering by the lobe, resulting in decrease in the form factor and an increase in  $P_{noi}(k)$ . The minimum  $k$  with full sensitivity is

$$k_{min} = \frac{2\pi D_{min}/\lambda}{d_T(z)} = 0.038h \text{ Mpc}^{-1} \frac{D_{min}/\lambda}{10m/0.525m} \frac{3.1Gpc}{d_T} \quad (31)$$

where  $D_{min}$  is the minimum cylinder or dish separation. For the numerical values of  $d_T$  and  $\lambda$  in this formula we have taken



**Fig. 5.** The  $P(k)$  and uncertainties for a four-month observation of  $2\pi sr$  at  $z = 1.5$  ( $\Delta z = 0.2$ ). The solid lines labeled  $P_{noi}$  give the noise power calculated with (30) for the three configurations of Figure 2. The dashed lines shows the SDSS  $P(k)$  at  $z \sim 0$  and extrapolated to  $z = 1.5$ . The dotted line shows the peak-to-peak amplitude of the BAOs at  $z = 1.5$ . The solid lines labeled  $\sigma_P$  shows the uncertainty in the measured power spectrum for  $\Delta k/k = 0.2$  calculated with (32) for configuration *a* and *b*. The vertical lines show the positions of the first four BAO peaks.

$z = 1.5$  ( $\Omega_M, \Omega_\Lambda = 0.27, 0.73$ ) and the  $D_{min}$  value for configurations *b* and *c* of Fig. 2. Figure 6 plots  $k_{min}(z)$  for  $D_{min} = 10m$  and  $D_{min} = 5m$ . To have good sensitivity at the first BAO peak,  $10m$  elements are acceptable at  $z = 1.5$  but smaller elements are needed at  $z = 0.5$ .

The uncertainty,  $\sigma_P$ , in the measured power spectrum averaged over an interval  $\Delta k$  is

$$\sigma_P = \frac{\langle W(\mathbf{k})^2 |\Gamma(\mathbf{k})|^4 \rangle^{1/2}}{\sqrt{N_{\Delta k}} \langle W(\mathbf{k}) \rangle} \quad (32)$$

where  $N_{\Delta k}$  is the number of modes in range  $\Delta k$  given by (7). If the noise dominates the power spectrum, this is

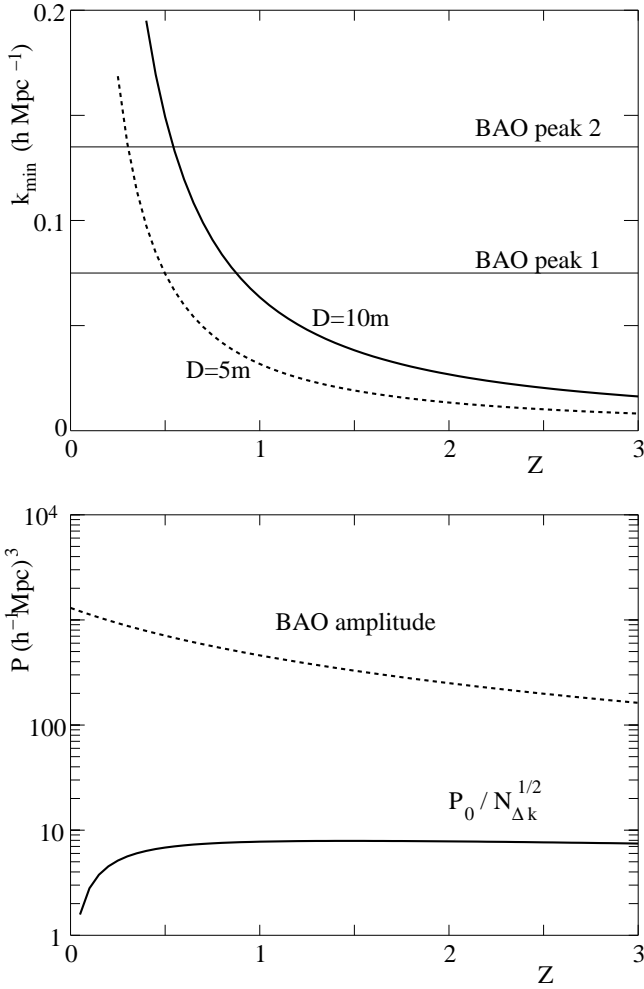
$$\sigma_P = \frac{P_0 \langle N_u(\mathbf{k})^2 \rangle^{1/2}}{\sqrt{N_{\Delta k}} \langle (\sum_u F(\mathbf{k}, \mathbf{u}))^2 \rangle} \quad (33)$$

Figure 5 shows the resolution  $\sigma_P$  calculated for a four-month observation of  $2\pi sr$  at  $z = 1.5$  ( $\Delta z = 0.2$ ) for the two cylinder configurations *a* and *b*, the dish configuration giving intermediate results. The resolution is less than the BAO amplitude shown in the figure. For the packed array *b*,  $P_{noi} < P_{LSS}$  at the first BAO peak so no improvement can be made by increasing the observing time. For the unpacked array *c*, increasing the observing time by a factor 10 would lead to a resolution similar to that for the packed array.

If  $P_{noi} > P_{LSS}$ ,  $\sigma_P$  is of order  $(P_0/N_u(\mathbf{k}))/\sqrt{N_{\Delta k}}$ . The value of this quantity for unpacked cylinders and calculated at the first BAO peak is plotted as a function of redshift in Fig. 6. Also shown is the peak-to-peak amplitude of the BAO oscillation. The resolution relative to the BAO amplitude rises slowly with redshift.

## 5. Radio sources

Extragalactic radio sources and Milky Way Synchrotron radiation have power law frequency spectra that allow them to be sub-



**Fig. 6.** The top panel shows the  $z$  dependence of  $k_{min} = 2\pi D/(\lambda d_T)$  for  $D = 10m$  (solid line) and  $D = 5m$  (dashed line). The two horizontal lines show the position of the first two BAO peaks. In the bottom panel, the solid line shows  $P_0/\sqrt{N_{\Delta k}}$  for an exposure of  $2\pi y r - sr$  cylinders in configuration *a*. The dashed line shows the BAO peak-to-peak amplitude at the first peak (lower panel).

tracted, in principle, from the HI spectrum. We consider here radiation for extragalactic sources because their random positions on the sky lead to a flux highly dependent on angular position. The radio source contribution to the sky brightness (4) is

$$T_{rs}(\alpha, \delta, \nu) = \frac{c^2}{2k_b \nu^2} \sum_i \Phi_i \left(\frac{\nu}{\nu_0}\right)^{-\gamma_i} \delta(\alpha - \alpha_i) \delta(\delta - \delta_i)$$

where the sum is over radio sources  $i$  of angular position  $(\alpha_i, \delta_i)$ , 1.42GHz flux (in Jy)  $\Phi_i$ , and spectral index is  $\gamma_i$ . The radio source power spectrum is determined by the Fourier transform:

$$\Gamma_{rs}(\mathbf{k}) = \frac{d_T^2 d_H (1+z)^2}{\bar{T}_{HI} \sqrt{V} \nu_0} \times \int d\alpha d\delta d\nu T_{rs}(\alpha, \delta, \nu) e^{-i(d_T k_\alpha \alpha + d_T k_\delta \delta + d_H (1+z)^2 k_z \nu / \nu_0)} \quad (34)$$

The  $\nu$  integral can be done by developing  $\nu^{-\gamma}$  to first order around the mean frequency in the box,  $\nu = \nu_0/(1+z)$ . The result is

$$\Gamma_{rs}(\mathbf{k}) = -i(-1)^n \exp(-id_z k_z / (1+z)) \quad (35)$$

$$\frac{d_T^2}{k_z \sqrt{V}} \frac{\Delta \nu}{\nu_0} (\gamma + 2)(1+z)^{\gamma+3} \frac{c^2}{2k_b \nu_0^2 \bar{T}_{HI}} \eta(k_\alpha, k_\delta)$$

where  $n = n_z$  is defined by (4),  $\gamma \sim 0.7$  is the mean spectral index (Binney & Merrifield 1998), and  $\eta$  is a sum over the radio sources in the angular region  $\Delta\alpha\Delta\delta$ :

$$\eta(k_\alpha, k_\delta) = (\gamma + 2)^{-1} \sum_i (\gamma_i + 2)(1+z)^{\gamma_i - \gamma} \Phi_i e^{-id_T(k_\alpha \alpha + k_\delta \delta)} \quad (36)$$

(Note:  $z$  is the redshift of the box, not of the radio source). The power in the mode  $\mathbf{k}$  is then

$$|\Gamma_{rs}(\mathbf{k})|^2 = \frac{d_T^2}{k_z^2 d_H} \Delta z (\gamma + 2)^2 (1+z)^{2(\gamma+1)} \left(\frac{c^2}{2k_b \nu_0^2 \bar{T}_{HI}}\right)^2 \Delta\Omega^{-1} |\eta(k_\alpha, k_\delta)|^2 \quad (37)$$

This spectrum is highly anisotropic because fluxes are correlated in frequency but not in angular direction.

The expectation value of  $|\eta|^2$  is

$$\Delta\Omega^{-1} \langle |\eta(k_\alpha, k_\delta)|^2 \rangle = \int_0^\infty d\Phi \frac{dN}{d\Phi d\Omega} \Phi^2 \sim 67.7 \text{ Jy}^2 \text{ sr}^{-1} \quad (38)$$

where we use the spectrum from Jackson (2004). Half of the integral comes from the  $\sim 5000$  sources per steradian with fluxes greater than 0.06Jy. This gives

$$\frac{c^2}{2k_b \nu_0^2} \left(\Delta\Omega^{-1} \langle |\eta(k_\alpha, k_\delta)|^2 \rangle\right)^{1/2} \sim 0.000133 \text{ K} \quad (39)$$

For  $z = 1.5$ ,  $\gamma = 0.7$ ,  $\Delta z = 0.2$  we then have

$$\langle |\Gamma_{rs}(\mathbf{k})|^2 \rangle = 7.0 \times 10^6 (h^{-1} \text{ Mpc})^3 \left(\frac{0.075 h \text{ Mpc}^{-1}}{k_z}\right)^2 \quad (40)$$

where the average is over  $(k_\alpha, k_\delta)$  at fixed  $k_z$ . Since this is considerably larger than  $P_{noi}$  and  $P_{LSS}$ ,  $\Gamma_{rs}(\mathbf{k})$  must be subtracted from the measured  $\Gamma(\mathbf{k})$  for each  $\mathbf{k}$ . This can be done by fitting the observed  $\Gamma(\mathbf{k})$  with the  $f(k_\alpha, k_\delta)/k_z$  form given by (35). In principle, this subtraction can be done with a precision  $\sigma_\Gamma \sim P_{noi}/\sqrt{N_z}$  where  $N_z$  is the number of radial modes over which the determination of  $\Gamma_{rs}$  is made. If this precision can be reached in practice, the subtracted power spectrum is not degraded below the spectrum in the absence of radio sources.

## 6. Sensitivity to cosmological parameters

In Sec. 4, we studied the impact of the various telescope configurations on power spectrum reconstruction. Fig. 5 shows the various power spectra, and it allows us to rank visually the configurations in terms of electronics noise fraction. The differences in  $P_{noi}$  will translate into differing precisions in the reconstruction of the BAO peak positions and in the estimation of cosmological parameters.

### 6.1. BAO peak precision

In order to estimate the precision with which BAO peak positions can be measured, we have generated power spectra that are the sum of the expected HI power spectra and the noise spectra calculated in the Section 4.1. The peaks in the generated spectra were then determined by a fitting procedure and the reconstructed peak positions compared with the generated peak positions.

To this end, we used a method similar to the one established in Blake and Glazebrook (2003). We generated power spectra for slices of Universe with a half-sky coverage and a redshift depth,  $\Delta z = 0.2$  for  $0 < z < 1.6$ . The power spectrum used in the simulation is the sum of HI signal term, corresponding to (41) and noise term derived from (26). The simulated power spectra HI is:

$$\frac{P_{HI}(k_{\perp}, k_{\parallel})}{P_{ref}(k_{\perp}, k_{\parallel})} = 1 + A k \exp(-k/\tau)^{\alpha} \sin\left(2\pi \sqrt{\frac{k_{\perp}^2}{k_{BAO\perp}^2} + \frac{k_{\parallel}^2}{k_{BAO\parallel}^2}}\right) \quad (41)$$

where  $k = \sqrt{k_{\perp}^2 + k_{\parallel}^2}$ , the parameters  $A$ ,  $\alpha$  and  $\tau$  are adjusted to the formula presented in Eisenstein and Hu (1998).  $P_{ref}(k_{\perp}, k_{\parallel})$  is the envelop curve of the HI power spectrum without baryonic oscillations. The parameters  $k_{BAO\perp}$  and  $k_{BAO\parallel}$  are the inverses of the oscillation periods in  $k$ -space. In the simulations, we used the following values for these parameters:  $A = 1.0$ ,  $\tau = 0.1 \text{ hMpc}^{-1}$ ,  $\alpha = 1.4$  and  $k_{BAO\perp} = k_{BAO\parallel} = 0.060 \text{ hMpc}^{-1}$ .

Each simulation is performed for a given set of parameters which are: the system temperature,  $T_{sys}$ , an observation time,  $T_{obs}$ , an average redshift and a redshift depth,  $\Delta z = 0.2$ . Then, each simulated power spectrum is fitted with a two dimensional normalized function  $P_{tot}(k_{\perp}, k_{\parallel})/P_{ref}(k_{\perp}, k_{\parallel})$  which is the sum of the signal power spectrum of (41) and the normalized noise power spectrum defined by (26) multiplied by a linear term,  $a_0 + a_1 k$ . The upper limit  $k_{max}$  in  $k$  of the fit corresponds to the approximate position of the linear/non-linear transition. This limit is established on the basis of the criterion discussed in Blake and Glazebrook (2003). In practice, we used for the redshifts  $z = 0.5$ ,  $1.1$  and  $1.5$  respectively  $k_{max} = 0.145 \text{ hMpc}^{-1}$ ,  $0.19 \text{ hMpc}^{-1}$  and  $0.23 \text{ hMpc}^{-1}$ .

Figure 7 shows the result of the fit for one of these simulations. Figure 8 histograms the recovered values of  $k_{BAO\perp}$  and  $k_{BAO\parallel}$  for 100 simulations. The widths of the two distributions give an estimate the statistical errors.

In addition, in the fitting procedure, both the parameters modeling the signal  $A$ ,  $\tau$ ,  $\alpha$  and the parameter correcting the noise power spectrum ( $a_0, a_1$ ) are floated to take into account the possible ignorance of the signal shape and the uncertainties in the computation of the noise power spectrum. In this way, we can correct possible imperfections and the systematic uncertainties are directly propagated to statistical errors on the relevant parameters  $k_{BAO\perp}$  and  $k_{BAO\parallel}$ . By subtracting the fitted noise contribution to each simulation, the baryonic oscillations are clearly observed, for instance, on Fig. 9.

In our comparison of the various telescope configurations, we have considered the following cases for  $\Delta z = 0.2$  slices with  $0 < z < 1.6$ .

- *Simulation without electronics noise*: the errors of power spectrum are directly related to the number of modes in the  $\Delta z = 0.2$  slice of  $2\pi sr$  (7).
- *Unpacked cylinder array* (configuration a)
- *Packed cylinder array*: (configuration b).
- *Dish array*: (configuration c).

Table 1 summarizes the result. The ranking of the three configurations is the same as that which we can deduce from the noise levels in Fig. 5: the best sensitivity is obtained with the packed cylinder array, then with the packed dish array and finally with the unpacked cylinder array. However, none of the

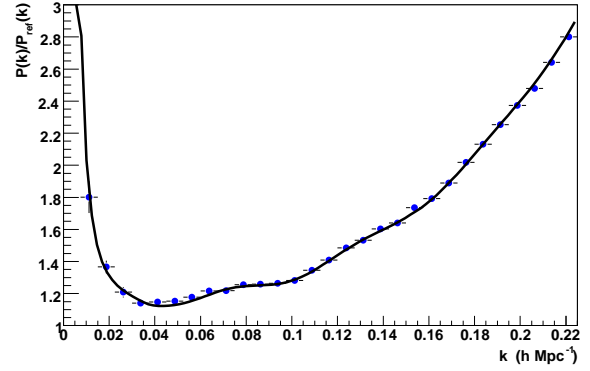


**Fig. 7.** 1D projection of the power spectrum for one simulation. The HI power spectrum is divided by an envelop curve  $P(k)_{ref}$  corresponding to the power spectrum without baryonic oscillations. The dots represents one simulation for a "packed" array of cylinders with a system temperature,  $T_{sys} = 50\text{K}$ , an observation time,  $T_{obs} = 4\text{month}$ , a solid angle of  $2\pi sr$ , an average redshift,  $z = 1.5$  and a redshift depth,  $\Delta z = 0.2$ . The solid line is the result of the fit to the data.

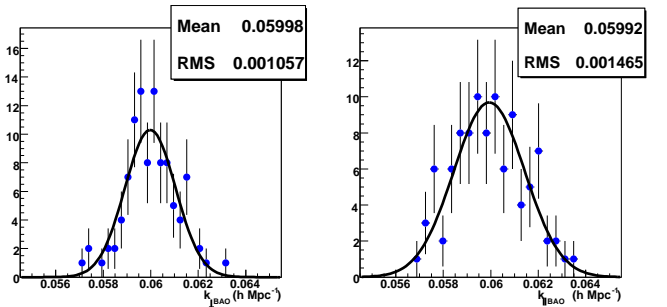


**Fig. 8.** Distributions of the reconstructed wavelength  $k_{BAO\perp}$  and  $k_{BAO\parallel}$  respectively, perpendicular and parallel to the line of sight for simulations as in Fig. 7. The fit by a Gaussian of the distribution (solid line) gives the width of the distribution which represents the statistical error expected on these parameters.

three configurations is limited by the cosmic variance with a four-month observation. As the errors scales with  $1/T_{obs}$ , configurations a) and c) could be significantly improved if the observation time is increased up to one year.

## 6.2. Expected sensitivity on $w_0$ and $w_a$

The observations give the HI power spectrum in angle-angle-redshift space rather than in real space. The inverse of the peak positions in the observed power spectrum therefore gives the angular and redshift intervals corresponding to the sonic horizon. The peaks in the angular spectrum are proportional to  $d_T(z)/s$  and those in the redshift spectrum to  $d_H(z)/s$ . The quantities  $d_T$ ,  $d_H$  and  $s$  all depend on the cosmological parameters. Figure 10 gives the angular and redshift intervals as a function of redshift for four cosmological models. The error bars on the lines for  $(\Omega_M, \Omega_\Lambda) = (0.27, 0.73)$  correspond to the expected errors on the peak positions taken from Table 1 for the four-month runs with the packed array. We see that with these uncertainties, the data would be able to measure  $w$  at better than the 10% level.

**Table 1.** Sensitivity on the measurement of  $k_{BAO\perp}$  and  $k_{BAO\parallel}$  as a function of the redshift  $z$  for various telescope configurations. 1<sup>st</sup> row: simulations without noise with pure cosmic variance; 2<sup>nd</sup> row: simulations with same electronics noise for a telescope in an unpacked cylinder array configuration a); 3<sup>th</sup> row: simulations with same electronics noise for a telescope in a packed cylinder array configuration b); 4<sup>th</sup> row: simulations with same electronics noise for a telescope in a packed dish array configuration c).

| $z$  |   | 0.1 | 0.3 | 0.5 | 0.7 | 0.9 | 1.1  | 1.3  | 1.5  |
|--|---|-----|-----|-----|-----|-----|------|------|------|
| <b>No Noise</b>  | $\sigma(k_{BAO\perp})/k_{BAO\perp}$ (%)         | 16  | 4.5 | 2.3 | 1.6 | 1.1 | 0.90 | 0.79 | 0.73 |
|  | $\sigma(k_{BAO\parallel})/k_{BAO\parallel}$ (%) | 18  | 5.8 | 3.1 | 2.3 | 1.6 | 1.3  | 1.2  | 1.1  |
| <b>a) Unpacked cylinder array</b><br>(4-months/redshift) | $\sigma(k_{BAO\perp})/k_{BAO\perp}$ (%)         | -   | -   | 19  | 16  | 12  | 9.8  | 9.3  | 9.8  |
|  | $\sigma(k_{BAO\parallel})/k_{BAO\parallel}$ (%) | -   | -   | 24  | 24  | 15  | 12   | 11   | 11   |
| <b>b) Packed cylinder array</b><br>(4-months/redshift)   | $\sigma(k_{BAO\perp})/k_{BAO\perp}$ (%)         | -   | 9.0 | 3.2 | 2.1 | 1.6 | 1.6  | 1.7  | 1.9  |
|  | $\sigma(k_{BAO\parallel})/k_{BAO\parallel}$ (%) | -   | 15  | 6.3 | 3.8 | 2.4 | 2.2  | 2.4  | 2.6  |
| <b>c) Packed Dish array</b><br>(4-months/redshift)       | $\sigma(k_{BAO\perp})/k_{BAO\perp}$ (%)         | -   | 11  | 7.2 | 6.5 | 5.7 | 5.5  | 5.5  | 5.6  |
|  | $\sigma(k_{BAO\parallel})/k_{BAO\parallel}$ (%) | -   | 24  | 11  | 8.6 | 6.7 | 6.4  | 6.9  | 6.9  |
| <b>b) Packed cylinder array</b><br>(4-year optimized)    | $\sigma(k_{BAO\perp})/k_{BAO\perp}$ (%)         | -   | -   | 2.0 | 1.5 | 1.1 | 1.1  | 1.0  | 1.1  |
|  | $\sigma(k_{BAO\parallel})/k_{BAO\parallel}$ (%) | -   | -   | 4.3 | 2.7 | 1.7 | 1.6  | 1.4  | 1.4  |

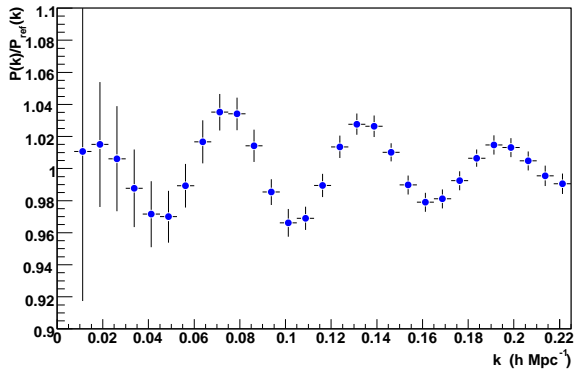


**Fig. 9.** 1D projection of the power spectrum averaged over 100 simulations of the packed cylinder array *b*. The simulations are performed for the following conditions: a system temperature,  $T_{sys} = 50K$ , an observation time,  $T_{obs} = 1$  year, a solid angle of  $2\pi sr$ , an average redshift,  $z = 1.5$  and a redshift depth,  $\Delta z = 0.2$ . The HI power spectrum is divided by an envelop curve  $P(k)_{ref}$  corresponding to the power spectrum without baryonic oscillations and the background estimated by a fit is subtracted. The errors are the RMS of the 100 distributions for each  $k$  bin and the dots are the mean of the distribution for each  $k$  bin.

To estimate the sensitivity to parameters describing dark energy equation of state, we follow the procedure explained in Blake and Glazebrook (2003). We can introduce the equation of state of dark energy,  $w(z) = w_0 + w_a \cdot z/(1+z)$  by replacing  $\Omega_\Lambda$  in the definition of  $d_T(z)$  and  $d_H(z)$ , (2) by:

$$\Omega_\Lambda = \Omega_\Lambda^0 \exp \left[ 3 \int_0^z \frac{1+w(z')}{1+z'} dz' \right] \quad (42)$$

where  $\Omega_\Lambda^0$  is the present-day dark energy fraction with respect to the critical density. Using the relative errors on  $k_{BAO\perp}$  and  $k_{BAO\parallel}$  given in Tab. 1, we can compute the Fisher matrix for five cosmological parameter:  $(\Omega_m, \Omega_b, h, w_0, w_a)$ . Then, the combination of this BAO Fisher matrix with the Fisher matrix obtained for Planck mission, allows us to compute the errors on dark energy parameters. The Planck Fisher matrix is obtained for the 8 parameters (assuming a flat universe):  $\Omega_m, \Omega_b, h, w_0, w_a, \sigma_8, n_s$  (spectral index of the primordial power spectrum) and  $\tau$  (optical depth to the last-scatter surface). The expected errors and the Figure of Merit, the inverse of the area in the 95% confidence

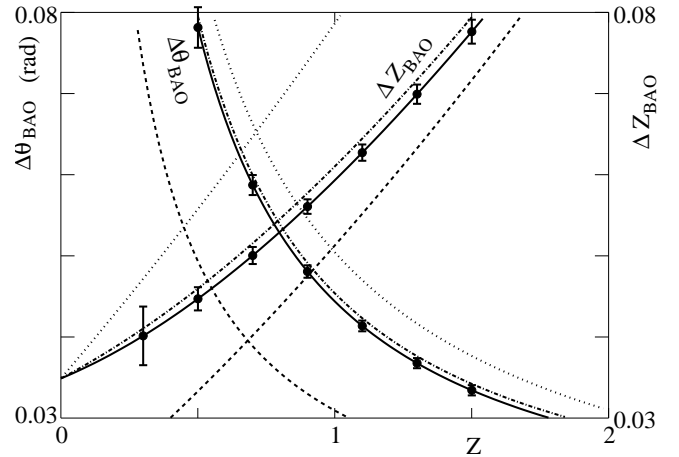


**Fig. 10.** The two “Hubble diagrams” for BAO experiments. The four falling curves give the angular size of the acoustic horizon (left scale) and the four rising curves give the redshift interval of the horizon (right scale). The solid lines are for  $(\Omega_M, \Omega_\Lambda, w) = (0.27, 0.73, -1)$ , the dashed for  $(1, 0, -1)$  the dotted for  $(0.27, 0, -1)$ , and the dash-dotted for  $(0.27, 0.73, -0.9)$ . The error bars on the solid curve correspond to the four-month run (packed array) of Table 1.

level contours (see Fig. 11) are summarized in Tab. 2. The ranking between the various configurations in terms of performances is consistent with the level of electronics noise observed on the power spectra of Fig. 5.

For an optimized project over a redshift range,  $0.4 < z < 1.6$ , with a total observation time of 4 years, the packed cylinders have a precision of 6% on  $w_0$  and 25% on  $w_a$ . Finally, Fig. 12 shows a comparison of different BAO projects, with a set of priors on  $(\Omega_m, \Omega_b, h)$  corresponding to the expected precision on these parameters in early 2010’s. This BAO project based on HI intensity mapping is clearly competitive with the next generation of optical surveys such as SDSS-III (SDSS-III 2008) or WFMOS (Basset et al. 2005).

## 7. Conclusion

In this paper we have discussed the measurement of the HI power spectrum with interferometric surveys. By presenting a simplified procedure for reconstructing the Fourier space map of



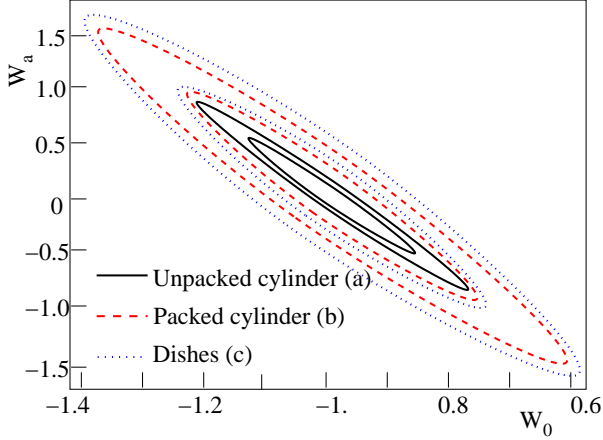


**Fig. 11.**  $1\sigma$  and  $2\sigma$  confidence level contours in the parameter plane ( $w_0, w_a$ ) for three configurations : a) unpacked array of north-south oriented cylinders (black line), b) packed array of north-south oriented cylinders (blue line) and c) packed array of dishes (red line).

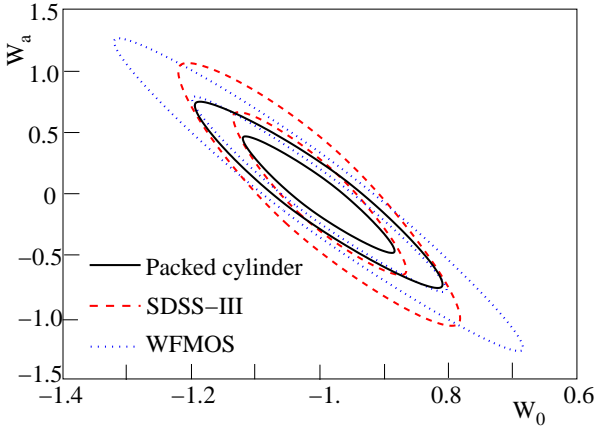


**Fig. 12.**  $1\sigma$  and  $2\sigma$  confidence level contours in the parameter plane ( $w_0, w_a$ ) for three BAO projects: WFMOS project (blue dotted line), SDSS-III (red dashed line) and packed cylinder array with HI intensity mapping (black solid line).

**Table 2.** Sensitivity on  $w_0$  and  $w_a$  and Figure of Merit (FoM) for various telescope configurations. 1<sup>st</sup> row: simulations without noise with pure cosmic variance; 2<sup>nd</sup> row: simulations with same electronics noise for a telescope in an unpacked cylinder array configuration a); 3<sup>th</sup> row: simulations with same electronics noise for a telescope in a packed cylinder array configuration b); 4<sup>th</sup> row: simulations with same electronics noise for a telescope in a packed dish array configuration c); 6<sup>th</sup> row: Configuration b) for an optimized 4-year survey with  $0.4 < z < 1.6$ .

|                                 | $\sigma(w_0)$ | $\sigma(w_a)$ | FoM (95%)  |
|---------------------------------|---------------|---------------|------------|
| No Noise                        | 0.059         | 0.24          | 136        |
| a) Unpacked cylinder array      | 0.17          | 0.69          | 10.1       |
| b) Packed cylinder array        | 0.091         | 0.36          | 69.1       |
| c) Packed Dish array            | 0.15          | 0.64          | 13.6       |
| Packed cylinder array - 4 years | <b>0.063</b>  | <b>0.25</b>   | <b>119</b> |

the GHz sky, we derived expressions for the noise power spectrum. Adding this spectrum to the expected HI power spectrum, we determined with what precision the positions of the BAO peaks can be measured. This led to a sensitivity to cosmological parameters that is competitive with other BAO projects.

In calculating the noise power spectrum, we considered three interferometer arrays using cylinders or dishes. Packed-cylinder and packed-dish arrays have comparable noises so the choice for one or the other must be based on cost and technical considerations, with cylinder arrays having simpler mechanical design but requiring more receivers.

*Acknowledgements.* We thank J.B. Peterson and U.-L. Pen for triggering our interest in cosmological HI interferometry and for many interesting discussions.

## References

- Abdalla, F.B. & Rawlings, S. 2005, MNRAS, 360, 27  
 Albrecht, A., Bernstein, G., Cahn, R. *et al.* (Dark Energy Task Force) 2006, arXiv:astro-ph/0609591  
 Barkana, R., and Loeb, A. 2007, Rep. Prog. Phys, 70 627  
 Bassett, B.A., Nichol, B., & Eisenstein, D.J. 2005, Astr. & Geoph., 46, 5.26-5.29  
 Binney, J. & Merrifield, M. 1998, Galactic Astronomy. (Princeton Univ. Press, Princeton)  
 Blake, C. & Glazebrook, K. 2003, ApJ, 594, 665; Glazebrook, K. & Blake, C. 2005 ApJ, 631, 1  
 Bowman, J. D., Barnes, D.G., Briggs, F.H. *et al* 2007, AJ, 133, 1505-1518  
 Chang, T., Pen, U.-L., Peterson, J.B. & McDonald, P. 2008, Phys. Rev. Lett., 100, 091303  
 Cole, S. Percival, W.J., Peacock, J.A. *et al.* (the 2dFGRS Team) 2005, MNRAS, 362, 505  
 Eisenstein, D.J. & Hu, W. 1998, ApJ, 496, 605  
 Eisenstein D. J., Zehavi, I., Hogg, D.W. *et al.*, (the SDSS Collaboration) 2005, ApJ, 633, 560  
 Furlanetto, S., Peng Oh, S. & Briggs, F. 2006, Phys. Rep., 433, 181-301  
 Hinshaw, G., Weiland, J.L., Hill, R.S. *et al.* 2008, arXiv:0803.0732)  
 Jackson, C.A. 2004, New A, 48, 1187  
 Mautkopf, P. D., Ade, P. A. R., de Bernardis, P. *et al.* 2000, ApJ, 536, 59  
 Percival, W.J., Nichol, R.C., Eisenstein, D.J. *et al.*, (the SDSS Collaboration) 2007, ApJ, 657, 645  
 Peterson, J.B., Bandura, K., & Pen, U.-L. 2006, arXiv:astro-ph/0606104  
 Rottgering H.J.A., Braun, r., Barthel, P.D. *et al.* 2006, arXiv:astro-ph/0610596  
 SDSS-III 2008, <http://www.sdss3.org/collaboration/description.pdf>  
 Tegmark, M., Blanton, M.R., Strauss, M. A. *et al.* 2004, ApJ, 606, 702  
 Tegmark, M. & Zaldarriaga, M. 2008, arXiv:0802.1710  
 Wolfe, A. M., Gawiser, E. & Prochaska, J.X. 2005 ARA&A, 43, 861  
 Wyithe, S., Loeb, A. & Geil, P. 2007 <http://fr.arxiv.org/abs/0709.2955>, submitted to MNRAS  
 Zwaan, M.A., Meyer, M.J., Staveley-Smith, L., Webster, R.L. 2005, MNRAS, 359, L30